

High-Resolution Distance Dependence Interrogation of Scanning Ion Conductance Microscopic Tip-Enhanced Raman Spectroscopy Enabled by Two-Dimensional Molybdenum Disulfide Substrates

Xing He, Abu Montakim Tareq, Kai Qi, Ylli Conti, Vincent Tung, and Naihao Chiang*



Cite This: *Nano Lett.* 2024, 24, 13805–13810



Read Online

ACCESS |



Metrics & More



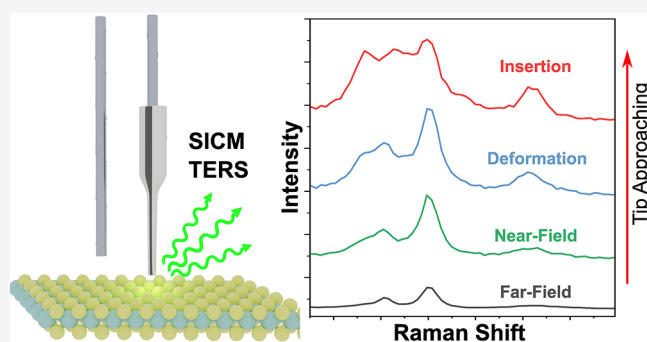
Article Recommendations



Supporting Information

ABSTRACT: Scanning ion conductance microscopy (SICM) is a powerful surface imaging tool used in the electrolytic environment. Tip-enhanced Raman spectroscopy (TERS) can give more information in addition to the morphology provided by the SICM by utilizing label-free Raman spectroscopy aided by the localized plasmonic enhancement from the metal-coated probes. In this study, the integration of SICM with TERS is demonstrated through employing a silver-coated plasmonic nanopipette. Leveraging a two-dimensional (2D) molybdenum disulfide (MoS_2) as a model system, the SICM-TERS enhancement factor was estimated to be $\sim 10^5$, supported by finite-difference time-domain (FDTD) simulation. Moreover, the subnanometer distance dependence SICM-TERS study reveals the tensile stress and structural changes caused by the nanopipette. These findings illustrate the potential of SICM-TERS for providing comprehensive morphological and chemical insights into electrolytic environments, paving the way for future investigations of electrocatalytic and biological systems.

KEYWORDS: Tip-Enhanced Raman Spectroscopy, Scanning-Ion Conductance Microscopy, Two-Dimensional Materials, Plasmonic Sensing

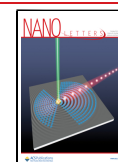


Scanning probe microscopy (SPM) is known for its well-established capability of imaging and manipulating surfaces with an unprecedented spatial resolution. In the family of SPMs, only two are suitable for imaging soft samples, such as biological systems, under controlled liquid environments: atomic force microscopy (AFM) with ultrasoft probes¹ and scanning ion-conductance microscopy (SICM).² While the external force native to AFM can be used to provide mechanical stimuli and induce biological processes such as ion-channel regulation³ and bioluminescence,⁴ the conformation of small surface molecules is likely to be altered, resulting in a diminished spatial resolution for live-sample imaging.⁵ In SICM, a glass nanopipette is employed as the scanning tip, enabling nondistorted, nondestructive nanoscale imaging of the biological surfaces in liquid environments *via* changes in the ionic current between the nanopipette and a reference electrode. Thus far, SICM has been applied for direct observation of single active ion channels,⁶ tracking of small-molecule migration,⁷ detection of single-stranded DNA,⁸ nanoscale biopsies,⁹ and patch-clamp electrophysiology measurements.¹⁰ This technique provides a unique opportunity to study interfacial phenomena under biologically relevant environments with <5 nm spatial resolution.¹¹

However, similar to other SPMs, SICM primarily provides topological information about the samples and ionic current cannot be used to investigate the chemical specificity of surface features. For example, surface proteins appear as bright protrusions in SICM images, but specific proteins cannot be chemically identified by using this technique. On the contrary, rich and detailed chemical information about the system of interest can be obtained via Raman spectroscopy, a label-free vibrational spectroscopic technique. Despite the many benefits Raman spectroscopy has for evaluating and probing biological systems (label-free, no water background in the fingerprint regions, sensitive to structural and environmental changes, etc.), a low signal-to-noise (S/N) ratio and diffraction-limited resolution have hindered its application in biological research.

Surface-enhanced Raman spectroscopy (SERS) overcomes the low S/N ratio challenge by amplifying and localizing the

Received: August 28, 2024
Revised: October 16, 2024
Accepted: October 16, 2024
Published: October 21, 2024



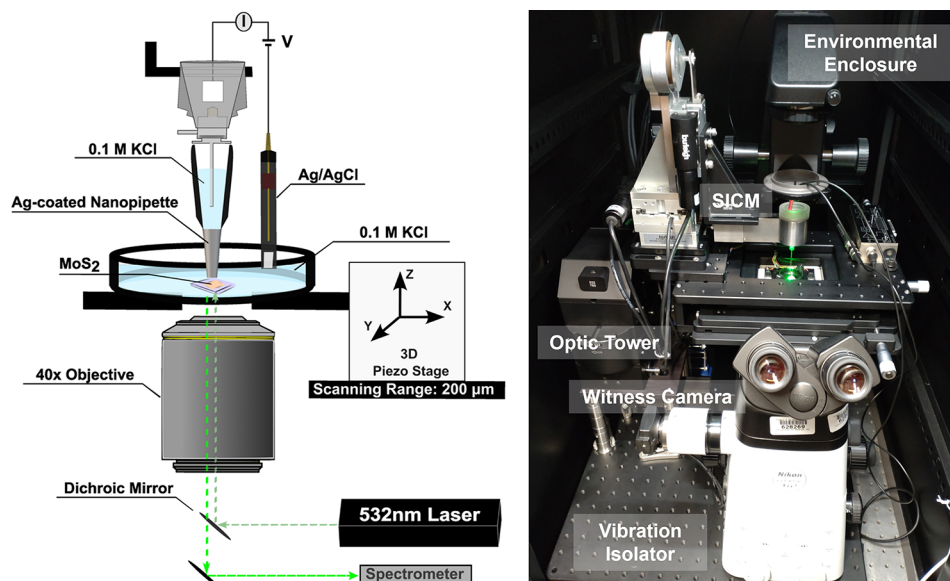


Figure 1. Schematic (left) and photograph (right) of the SICM-TERS setup. The monolayer MoS₂ is placed at the bottom of a Petri dish filled with 0.1 M KCl solution. A silver-coated nanopipette is immersed into the solution from the top. A 532 nm continuous laser is focused from the bottom onto the tip apex through a 40× long working distance objective lens. The TERS signal is collected with the same objective lens in a backscattering geometry.

electromagnetic fields of plasmonic nanostructures. The scanning probes are naturally in the nanometer regime and can provide the needed electromagnetic enhancement if they are fabricated with plasmonic metals. This joint SPM and SERS approach is termed tip-enhanced Raman spectroscopy (TERS), which combines the atomic spatial resolution of SPMs with the single-molecule chemical sensitivities of SERS.¹² Under ultrahigh vacuum (UHV) conditions, UHV-TERS has demonstrated Ångström-scale spatial resolution^{13–16} and has given new insights into surface molecule orientation¹³ and molecule–molecule interaction.¹⁷ Recently, TERS has been extended into the solution phase with AFM^{18,19} and electrochemical AFM/STM.^{20–24} If this unprecedented spatial resolution can be realized in the liquid environment, it is an ideal identification and spatial mapping technique in the three dimensions of soft materials.

Herein, SICM-TERS on a two-dimensional (2D) molybdenum disulfide (MoS₂) was demonstrated in an ionic environment using a silver-coated nanopipette. Inspired by the previously demonstrated AFM-TERS and SICM setups,^{25,26} a custom-built SICM is mounted on an inverted optical microscope to enable Raman spectroscopic detection at the SICM probe apex in a backscattering geometry (Figure 1). A three-dimensional inchworm motorized stage controls the nanopipette position and aligns it to the laser focus. A piezoflexure nanostage is used to achieve the precise and fast response required for SICM imaging and feedback.

A TERS enhancement factor of $\sim 10^5$ has been observed in the non-gap-mode geometry when the tip is in close proximity to the MoS₂ surface. Additionally, Raman mode shifting and splitting have also been observed when the nanopipet moved toward the 2D MoS₂ film and eventually inserted into the film. The highly structurally sensitive TERS signals enable the characterization of SICM working distance and the interaction between the probe and the surface at the subnanometer scale.

In a TERS experiment, the plasmonic properties of the SPM probes are important. For the presented SICM-TERS, the

nanopipette was pulled by a CO₂ laser puller (P-2000, Sutter Instrument) using a quartz capillary with an outer diameter of 1.0 mm and inner diameter of 0.7 mm (Sutter Instrument). After the nanopipette was made, a high vacuum sputter coater (VTC-16-3HD, MTI Corporation, modified with a Varian TPS-compact turbo pumping station; the base pressure was $\sim 5 \times 10^{-5}$ Torr) was used to sputter the pipet with 25 nm of silver on one side in an argon environment at 4.5×10^{-3} Torr held at 120 °C. The SEM images were acquired with a Phenom pharos G2 Desktop FEG-SEM (ThermoFisher Scientific). Figure 2a,b

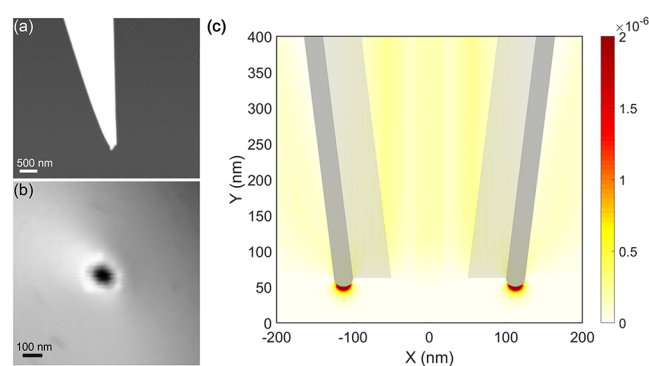


Figure 2. (a) and (b) SEM images of the nanopipette tip at 45° (a) and 90° (b) cross-sectional angles. (c) FDTD simulation of the electric field power density around the nanopipette. The glass part of the pipet is shown in light gray, while the silver coating is shown in dark gray. On the end of the pipet, there are two hemispheres to mimic the silver extension part, as shown in (a).

shows representative scanning electron microscopy (SEM) cross-section images of a silver-sputtered SICM-TERS nanopipette at 45 and 90° angles, respectively. The opening of the nanopipette tip is around 50 nm in radius, estimated by the SEM images. The SEM image represents a direct view of the nanopipette, but it needs to be broken for mounting. Since the nanopipette opening directly correlates with the total

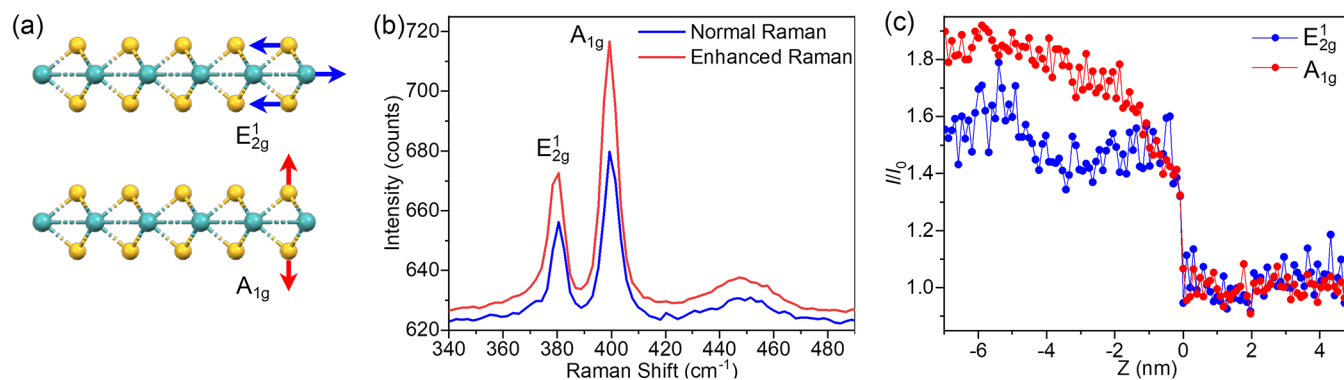


Figure 3. (a) Illustration of two Raman modes of the MoS₂ monolayer (the in-plane vibration E_{2g}^1 and the out-of-plane motion A_{1g}). (b) Normal Raman (blue solid line) and SICM-TERS Raman (red solid line) spectra. (c) Raman mode intensity as a function of the distance between the tip and the MoS₂ monolayer. The zero position of Z is set to the distance at which the intensity change begins.

resistance,²⁷ a current–voltage (I – V) curve has been performed for the conductance measurement (Figure S1 in the Supporting Information). The calculation based on an established model^{28,29} shows the inner pipet radius to be ~ 45 nm, which agrees with the SEM image estimation.

The custom-built SICM-TERS performed in this study uses transparent and insulating samples mounted on an inverted microscope. The longitudinal mode from a tightly focused linearly polarized laser excitation enables the excitation of the plasmon at the tip apex.^{30–32} Therefore, neither gap-mode plasmon couplings nor quantum tunneling is expected. The near-field responses of the silver-coated plasmonic nanopipette can be simulated with computational classical electrodynamics.^{33,34} The simulated nanopipette geometry is based on the parameters extracted from the SEM images. The computation region is filled with water (refractive index 1.31) to account for the plasmon red-shifts in liquids.³⁵ Furthermore, since the majority of the enhanced Raman signal was attributed to the hot spot with the strongest enhancement,³⁶ two hemispheres of silver were added on the tip apex to mimic the Ag protrusions seen in the SEM image (Figure 2a). The simulated electric field power density ($|E|^2$) shows that the electric field is primarily enhanced near the silver hemispheres (Figure 2c). The enhancement of $|E|^2$ is around 10^3 by comparing the tip apex part with the far away region, which gives an $\sim 10^6$ TERS enhancement factor considering the Raman signal enhancement is proportional to $|E|^4$.³⁷

Monolayer MoS₂, a versatile material for electronics, photonics, and electrocatalysis,^{38–40} is used as a proof-of-concept system for SICM-TERS. The bandgap of the 2D MoS₂ matches the green spectral region; therefore, the material has a large resonance Raman cross-section when excited with a green laser. The growth of monolayer MoS₂ films on sapphire substrates by the conventional chemical vapor deposition method and the PMMA-transfer method were described in previous studies.^{39,41} Figure 3a illustrates the two major MoS₂ Raman modes, E_{2g}^1 (385 cm^{-1}) and A_{1g} (402 cm^{-1}), representing the in-plane vibration of both molybdenum and sulfur atoms and the out-of-plane vibration of sulfur atoms, respectively.^{42–44} The normal Raman spectrum of MoS₂ was measured (blue solid line in Figure 3b) when the pipet tip was far from the surface. As the Ag-coated nanopipette approaches the MoS₂ sample, the Raman spectrum is enhanced, as shown by the red solid line in Figure 3b.

The Raman signal enhancement happens at such a small distance that the changes show a sudden jump, even with the 0.1 nm step size of the sample movement (Figure 3b). Moreover, the in- and out-of-plane Raman modes behave slightly differently. The intensity enhancement of the out-of-plane mode (A_{1g}) appears to be higher than that of the in-plane mode (E_{2g}^1), which can be attributed to the electric field around the silver-coated tip that is vertically closer to the conductor surface, as it satisfies the boundary conditions of Maxwell's equations. By the surface selection rule of TERS,⁴⁵ the out-of-plane modes align better with the plasmonic dipole at the tip–sample junction. Therefore, A_{1g} is preferably enhanced over the in-plane E_{2g}^1 mode. The same experiment was performed on an uncoated glass nanopipette, showing no Raman signal enhancement (Figure S4 in the Supporting Information).

Furthermore, the rich chemical information provided by Raman spectroscopy can be exploited to elucidate the effects that cause structural changes. Specifically, the two MoS₂ Raman modes are sensitive to local strain introduced onto the materials, resulting in mode shifting and splitting.^{46,47} Figure 4a shows a waterfall plot of the SICM-TERS spectra when the surface approaches the tip with a step size of 0.1 nm. The distance-dependent SICM-TERS data show a clear signal enhancement as the tip–sample gap decreases. Moreover, a small Raman mode shift was observed in the first 0.5 nm (Figure 4b). Based on previously reported strain-induced shift values of MoS₂ Raman modes,⁴⁷ the strain caused by the nanopipette in the proximity of the materials is estimated to be ~ 0.2 – 0.4% , observing the shifts of E_{2g}^1 and A_{1g} modes, respectively. Even though SICM was known to cause less deformation than AFM,⁵ the MoS₂ SICM-TERS spectra indicate the Ag nanopipette still introduces a small amount of pressure within the extent of the plasmonic near-field.

However, when the sample moved even closer toward the tip (-0.6 to -1.1 nm), the splitting of the E_{2g}^1 peak was also observed besides the intensity enhancement. This result indicates the lifting of the degenerate E mode due to an increase of the tensile stress ($>0.8\%$)^{48–50} of the film, which is also observed with the AFM-TERS spectra of MoS₂.^{51,52} At this short distance, the plasmonic nanopipet introduces a non-negligible strain to the materials. A direct comparison with force-controlled EC-AFM-TERS would be ideal to further elucidate the strain effect of MoS₂ in electrolytic environments.

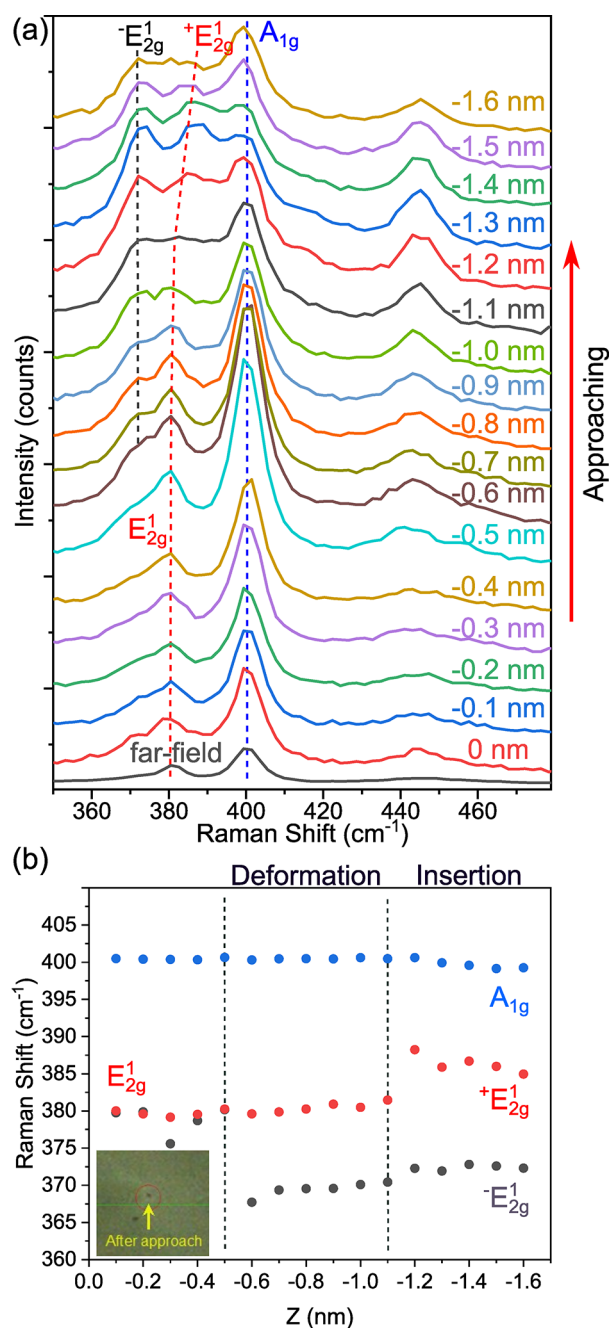


Figure 4. (a) SICM-TERS spectral evaluation of the MoS₂ monolayer while the nanopipette tip approaches the sample. The step size between the TERS spectra is 0.1 nm (excluding the bottom black far-field Raman spectrum). (b) MoS₂ Raman peak shifts as a function of the tip–sample distance extracted from (a). Inset: optical microscope image of the MoS₂ film after the experiment.

Possible tip insertion was observed by the SICM-TERS spectra, as the tip–sample gap further shrinks below -1.2 nm. The E_{2g}^1 mode further splits, and the signal of the A_{1g} mode decreases. The reduction of A_{1g} suggests that the tip has been inserted into MoS₂, and the most enhanced region has moved over passed materials. The silver island film on the shaft of the Ag-coated nanopipette enabled the detection of the disrupted materials in a tip-SERS fashion.⁵³ Moreover, the further split of E_{2g}^1 modes resembles the edge structure of MoS₂, suggesting the disruption of the materials caused by the downward-moving nanopipette. The process of the tip insertion lasts less

than 1 nm, according to Figure 4a, which is consistent with the thickness of monolayer MoS₂ (around 0.7 nm).⁵⁴ An optical micrograph shown in the inset of Figure 4b clearly shows a hole in the MoS₂ sample after the experiment.

The SICM-TERS enhancement factor (EF) can be evaluated based on the spectra shown in Figures 3 and 4, which have apparent signal enhancement EFs of 1.7 and 7.0, respectively. To estimate the SICM-TERS enhancement factor (EF_0), the tip and laser spot sizes must be considered. The laser beam size was measured to be about $1.7\ \mu\text{m}$ of full width at half maximum (fwhm) with the 40 \times objective lens (NA 0.6). With the pipet opening size of 100 nm in diameter and the coating tip about 25 nm in diameter, the EF has a relation with the SICM-TERS EF_0 as shown

$$EF = (1 - P) + EF_0 \times P \quad (1)$$

where P is the portion of the tip-enhanced laser compared to the whole laser beam, as calculated in the Supporting Information. Using eq 1, the SICM-TERS EF_0 is estimated to be $\sim 10^4$ to $\sim 10^5$, which suggests that the plasmonic resonances were the dominating enhancement mechanism rather than the lightning rod effect. This estimation does not take into account atomistic features that might be present on the tip apex, and it is likely to be underestimated, as the fine feature can further contribute to the electromagnetic field confinement. In principle, SICM-TERS resolution could be defined by the atomistic plasmonic nanostructures^{55,56} and therefore, it could exceed the SICM imaging resolution that depends on the nanopipette opening size. Moreover, many other factors might affect the enhanced electromagnetic field, such as absorbed ions between the tip and sample and electric double layers if a third electrode is connected to the sample. SICM-TERS can potentially elucidate these effects, complementing the observations from other EC-TERS measurements.

In conclusion, the capability of TERS is extended to a liquid environment within a SICM framework, marking a pioneering endeavor in the field. The experimentally observed SICM-TERS enhancement factor ($\sim 10^5$) is evaluated by leveraging a 2D MoS₂ sample as a proof-of-concept model and is supported by FDTD simulations. This simulation, even limited to classical theory, is sufficient to rule out other nonplasmonic mechanisms, but a more sophisticated high-level theoretical approach is needed as the liquid-phase TERS field progresses. Moreover, the strain-induced MoS₂ vibrational mode shifting and splitting reveal that the optimal working distance for SICM-TERS is between 0.4 and 1 nm above the surface without causing significant material deformation. This working distance of TERS is consistent with the recently reported values for UHV-TERS⁵⁷ and the short-range distance dependence of SERS.⁵⁸ The SICM-TERS spectral resolution achieved highlights its ability to provide detailed morphological and crucial chemical insights into the materials and methodology. Overall, this work not only underscores the synergistic potential of combining SICM with TERS but also sets the stage for its application in soft materials, electrocatalysis, and biological research exploiting solid–liquid interfaces.

■ ASSOCIATED CONTENT

Supporting Information

The Supporting Information is available free of charge at <https://pubs.acs.org/doi/10.1021/acs.nanolett.4c04200>.

Materials and methods, resistance measurement of the Ag nanopipets, SICM-TERS of MoS₂ with an uncoated glass nanopipet, SICM-TERS enhancement factor calculation, and computation input file for reported FDTD simulation (PDF)

AUTHOR INFORMATION

Corresponding Author

Naihao Chiang – Department of Chemistry, University of Houston, Houston, Texas 77204, United States;
orcid.org/0000-0003-3782-6546; Email: nchiang@uh.edu

Authors

Xing He – Department of Chemistry, University of Houston, Houston, Texas 77204, United States

Abu Montakim Tareq – Department of Chemistry, University of Houston, Houston, Texas 77204, United States;
orcid.org/0000-0003-2704-7610

Kai Qi – Department of Chemical System Engineering, The University of Tokyo, Tokyo 113-8656, Japan

Ylli Conti – Institute of Materials Science of Barcelona (ICMAB-CSIC), Campus de la UAB, Bellaterra 08193, Spain; orcid.org/0000-0001-6714-922X

Vincent Tung – Department of Chemical System Engineering, The University of Tokyo, Tokyo 113-8656, Japan

Complete contact information is available at:

<https://pubs.acs.org/10.1021/acs.nanolett.4c04200>

Author Contributions

The experiments and characterization were led and designed by N.C. and X.H. with assistance of A.M.T.; Y.C. performed the electron microscopy characterizations. The MoS₂ fabrication was performed by K.Q. and V.T. The manuscript was prepared by X.H. and N.C. with contributions from all other coauthors.

Notes

The authors declare no competing financial interest.

ACKNOWLEDGMENTS

X.H., A.M.T., and N.C. acknowledge support from the National Institute of Biomedical Imaging and Bioengineering Grant R00EB028325. This work was partly completed with resources from the Research Computing Data Core at the University of Houston. We especially thank Jeffrey Sarlo for his help with the computing system. K.Q. and V.T. are indebted to the financial support from the University of Tokyo and the Japan Society for the Promotion of Science (JSPS, 23H00253). This work was supported by JST, CREST Grant Number JPMJCR24A3, Japan. We offer our deepest gratitude to Drs. Leonardo Scarabelli (University of Cantabria) and Gail Vinnacombe-Willson (CIC bioGUNE) for providing the necessary resources and support for this work.

REFERENCES

- (1) Ren, J.; Zou, Q. Adaptive-scanning, near-minimum-deformation atomic force microscope imaging of soft sample in liquid: Live mammalian cell example. *Ultramicroscopy* **2018**, *186*, 150–157.
- (2) Klenerman, D.; Korchev, Y.; Novak, P.; Shevchuk, A. Noncontact Nanoscale Imaging of Cells. *Annual Review of Analytical Chemistry* **2021**, *14*, 347–361.
- (3) Lee, W.; et al. Synergy between Piezo1 and Piezo2 channels confers high-strain mechanosensitivity to articular cartilage. *Proc. Natl. Acad. Sci. U. S. A.* **2014**, *111*, E5114–E5122.
- (4) Tesson, B.; Latz, M. I. Mechanosensitivity of a Rapid Bioluminescence Reporter System Assessed by Atomic Force Microscopy. *Biophys. J.* **2015**, *108*, 1341–1351.
- (5) Seifert, J.; Rheinlaender, J.; Novak, P.; Korchev, Y. E.; Schaffer, T. E. Comparison of Atomic Force Microscopy and Scanning Ion Conductance Microscopy for Live Cell Imaging. *Langmuir* **2015**, *31*, 6807–6813.
- (6) Korchev, Y. E.; Negulyaev, Y. A.; Edwards, C. R. W.; Vodyanov, I.; Lab, M. J. Functional localization of single active ion channels on the surface of a living cell. *Nat. Cell Biol.* **2000**, *2*, 616–619.
- (7) Leitao, S. M.; et al. Time-Resolved Scanning Ion Conductance Microscopy for Three-Dimensional Tracking of Nanoscale Cell Surface Dynamics. *ACS Nano* **2021**, *15*, 17613–17622.
- (8) Karhanek, M.; Kemp, J. T.; Pourmand, N.; Davis, R. W.; Webb, C. D. Single DNA Molecule Detection Using Nanopipets and Nanoparticles. *Nano Lett.* **2005**, *5*, 403–407.
- (9) Actis, P.; et al. Compartmental Genomics in Living Cells Revealed by Single-Cell Nanobiopsy. *ACS Nano* **2014**, *8*, 546–553.
- (10) Yang, X.; et al. Investigation of morphological and functional changes during neuronal differentiation of PC12 cells by combined Hopping Probe Ion Conductance Microscopy and patch-clamp technique. *Ultramicroscopy* **2011**, *111*, 1417–1422.
- (11) Leitao, S. M.; et al. Time-Resolved Scanning Ion Conductance Microscopy for Three-Dimensional Tracking of Nanoscale Cell Surface Dynamics. *ACS Nano* **2021**, *15*, 17613–17622.
- (12) Zrimsek, A. B.; et al. Single-Molecule Chemistry with Surface- and Tip-Enhanced Raman Spectroscopy. *Chem. Rev.* **2017**, *117*, 7583–7613.
- (13) Chiang, N.; et al. Conformational Contrast of Surface-Mediated Molecular Switches Yields Ångström-Scale Spatial Resolution in Ultrahigh Vacuum Tip-Enhanced Raman Spectroscopy. *Nano Lett.* **2016**, *16*, 7774–7778.
- (14) Lee, J.; Crampton, K. T.; Tallarida, N.; Apkarian, V. A. Visualizing vibrational normal modes of a single molecule with atomically confined light. *Nature* **2019**, *568*, 78–82.
- (15) Li, L.; et al. Angstrom-Scale Spectroscopic Visualization of Interfacial Interactions in an Organic/Borophene Vertical Heterostructure. *J. Am. Chem. Soc.* **2021**, *143*, 15624–15634.
- (16) Wang, R.-P.; et al. Sub-Nanometer Resolved Tip-Enhanced Raman Spectroscopy of a Single Molecule on the Si(111) Substrate. *J. Phys. Chem. C* **2022**, *126*, 12121–12128.
- (17) Chiang, N.; et al. Probing Intermolecular Vibrational Symmetry Breaking in Self-Assembled Monolayers with Ultrahigh Vacuum Tip-Enhanced Raman Spectroscopy. *J. Am. Chem. Soc.* **2017**, *139*, 18664–18669.
- (18) Mrdenović, D.; Ge, W.; Kumar, N.; Zenobi, R. Nanoscale Chemical Imaging of Human Cell Membranes Using Tip-Enhanced Raman Spectroscopy. *Angew. Chem., Int. Ed.* **2022**, *61*, No. e202210288.
- (19) Mrdenović, D.; et al. Regioselective Tip-Enhanced Raman Spectroscopy of Lipid Membranes with Sub-Nanometer Axial Resolution. *Nano Lett.* **2023**, *23*, 3939–3946.
- (20) Kang, G.; Yang, M.; Mattei, M. S.; Schatz, G. C.; Van Duyne, R. P. In Situ Nanoscale Redox Mapping Using Tip-Enhanced Raman Spectroscopy. *Nano Lett.* **2019**, *19*, 2106–2113.
- (21) Jiang, S.; et al. Investigation of Cobalt Phthalocyanine at the Solid/Liquid Interface by Electrochemical Tip-Enhanced Raman Spectroscopy. *J. Phys. Chem. C* **2019**, *123*, 9852–9859.
- (22) Fiocco, A.; et al. Electrochemical Tip-Enhanced Raman Spectroscopy for the Elucidation of Complex Electrochemical Reactions. *Anal. Chem.* **2024**, *96*, 2791–2798.
- (23) Huang, S.-C.; et al. Probing the Intermediate in the Electrochemical Reduction of Nitrobenzene Derivative by EC-TERS. *J. Phys. Chem. C* **2023**, *127*, 12568–12575.

- (24) Huang, S.-C.; et al. Electrochemical Tip-Enhanced Raman Spectroscopy with Improved Sensitivity Enabled by a Water Immersion Objective. *Anal. Chem.* **2019**, *91*, 11092–11097.
- (25) Mattei, M.; et al. Tip-Enhanced Raman Voltammetry: Coverage Dependence and Quantitative Modeling. *Nano Lett.* **2017**, *17*, 590–596.
- (26) Zhu, C.; Huang, K.; Siepser, N. P.; Baker, L. A. Scanning Ion Conductance Microscopy. *Chem. Rev.* **2021**, *121*, 11726–11768.
- (27) Perry, D.; Momotenko, D.; Lazenby, R. A.; Kang, M.; Unwin, P. R. Characterization of Nanopipettes. *Anal. Chem.* **2016**, *88*, 5523–5530.
- (28) Del Linz, S.; et al. Contact-Free Scanning and Imaging with the Scanning Ion Conductance Microscope. *Anal. Chem.* **2014**, *86*, 2353–2360.
- (29) Hall, J. E. Access resistance of a small circular pore. *J. Gen. Physiol.* **1975**, *66*, 531–532.
- (30) Novotny, L.; Sánchez, E. J.; Sunney Xie, X. Near-field optical imaging using metal tips illuminated by higher-order Hermite–Gaussian beams. *Ultramicroscopy* **1998**, *71*, 21–29.
- (31) Bouhelier, A.; Beversluis, M. R.; Novotny, L. Near-field scattering of longitudinal fields. *Appl. Phys. Lett.* **2003**, *82*, 4596–4598.
- (32) Hayazawa, N.; Saito, Y.; Kawata, S. Detection and characterization of longitudinal field for tip-enhanced Raman spectroscopy. *Appl. Phys. Lett.* **2004**, *85*, 6239–6241.
- (33) Johnson, S.; Oskooi, A.; Taflove, A. *Advances in FDTD Computational Electrodynamics: Photonics and Nanotechnology*; Artech: 2013.
- (34) Oskooi, A. F.; et al. Meep: A flexible free-software package for electromagnetic simulations by the FDTD method. *Comput. Phys. Commun.* **2010**, *181*, 687–702.
- (35) Willets, K. A.; Van Duyne, R. P. Localized Surface Plasmon Resonance Spectroscopy and Sensing. *Annu. Rev. Phys. Chem.* **2007**, *58*, 267–297.
- (36) Weber, M. L.; Willets, K. A. Correlated Super-Resolution Optical and Structural Studies of Surface-Enhanced Raman Scattering Hot Spots in Silver Colloid Aggregates. *J. Phys. Chem. Lett.* **2011**, *2*, 1766–1770.
- (37) Schatz, G. C.; Young, M. A.; Van Duyne, R. P. Electromagnetic Mechanism of SERS. In *Surface-Enhanced Raman Scattering: Physics and Applications*; Kneipp, K., Moskovits, M., Kneipp, H., Eds.; Springer Berlin Heidelberg: 2006; pp 19–45.
- (38) Aljarb, A.; et al. Ledge-directed epitaxy of continuously self-aligned single-crystalline nanoribbons of transition metal dichalcogenides. *Nat. Mater.* **2020**, *19*, 1300–1306.
- (39) Fu, J.-H.; et al. Oriented lateral growth of two-dimensional materials on c-plane sapphire. *Nat. Nanotechnol.* **2023**, *18*, 1289–1294.
- (40) Aljarb, A.; et al. Interfacial Reconstructed Layer Controls the Orientation of Monolayer Transition-Metal Dichalcogenides. *ACS Nano* **2023**, *17*, 10010–10018.
- (41) Yu, H.; et al. Wafer-Scale Growth and Transfer of Highly-Oriented Monolayer MoS₂ Continuous Films. *ACS Nano* **2017**, *11*, 12001–12007.
- (42) Bertrand, P. A. Surface-phonon dispersion of MoS₂. *Phys. Rev. B* **1991**, *44*, 5745–5749.
- (43) Lee, C.; et al. Anomalous Lattice Vibrations of Single- and Few-Layer MoS₂. *ACS Nano* **2010**, *4*, 2695–2700.
- (44) Li, H.; et al. From Bulk to Monolayer MoS₂: Evolution of Raman Scattering. *Adv. Funct. Mater.* **2012**, *22*, 1385–1390.
- (45) Mahapatra, S.; Schultz, J. F.; Ning, Y.; Zhang, J.-L.; Jiang, N. Probing surface mediated configurations of nonplanar regioisomeric adsorbates using ultrahigh vacuum tip-enhanced Raman spectroscopy. *Nanoscale* **2019**, *11*, 19877–19883.
- (46) Huang, T.-X.; et al. Probing the edge-related properties of atomically thin MoS₂ at nanoscale. *Nat. Commun.* **2019**, *10*, 5544.
- (47) Rice, C.; et al. Raman-scattering measurements and first-principles calculations of strain-induced phonon shifts in monolayer MoS₂. *Phys. Rev. B* **2013**, *87*, 81307.
- (48) Yan, Y.; et al. Tuning the physical properties of ultrathin transition-metal dichalcogenides via strain engineering. *RSC Adv.* **2020**, *10*, 39455–39467.
- (49) Panasci, S. E.; et al. Strain, Doping, and Electronic Transport of Large Area Monolayer MoS₂ Exfoliated on Gold and Transferred to an Insulating Substrate. *ACS Appl. Mater. Interfaces* **2021**, *13*, 31248–31259.
- (50) Wang, Y.; Cong, C.; Qiu, C.; Yu, T. Raman Spectroscopy Study of Lattice Vibration and Crystallographic Orientation of Monolayer MoS₂ under Uniaxial Strain. *Small* **2013**, *9*, 2857–2861.
- (51) Ma, X.; et al. Toward High-Contrast Atomic Force Microscopy-Tip-Enhanced Raman Spectroscopy Imaging: Nano-antenna-Mediated Remote-Excitation on Sharp-Tip Silver Nanowire Probes. *Nano Lett.* **2019**, *19*, 100–107.
- (52) Velický, M.; et al. Strain and Charge Doping Fingerprints of the Strong Interaction between Monolayer MoS₂ and Gold. *J. Phys. Chem. Lett.* **2020**, *11*, 6112–6118.
- (53) Touzalin, T.; Joiret, S.; Maisonhaute, E.; Lucas, I. T. Complex Electron Transfer Pathway at a Microelectrode Captured by in situ Nanospectroscopy. *Anal. Chem.* **2017**, *89*, 8974–8980.
- (54) Wang, Y.-T.; et al. Ultrafast Multi-Level Logic Gates with Spin-Valley Coupled Polarization Anisotropy in Monolayer MoS₂. *Sci. Rep.* **2015**, *5*, 8289.
- (55) Liu, P.; Chulhai, D. V.; Jensen, L. Single-Molecule Imaging Using Atomistic Near-Field Tip-Enhanced Raman Spectroscopy. *ACS Nano* **2017**, *11*, 5094–5102.
- (56) Zhang, Y.; Dong, Z.-C.; Aizpurua, J. Theoretical treatment of single-molecule scanning Raman picoscopy in strongly inhomogeneous near fields. *J. Raman Spectrosc.* **2021**, *52*, 296–309.
- (57) Zhang, J.-X.; et al. Probing the Vertical Resolving Ability of Tip-Enhanced Raman Spectroscopy. *ACS Photonics* **2023**, *10*, 3682–3690.
- (58) Masango, S. S.; et al. High-Resolution Distance Dependence Study of Surface-Enhanced Raman Scattering Enabled by Atomic Layer Deposition. *Nano Lett.* **2016**, *16*, 4251–4259.